Full length article

Evaluation of various multi-cell design concepts for crashworthiness design of thin-walled aluminum tubes

E. Acar[a], M. Altin[b], M.A. Güler[c,a,*]

[a] Department of Mechanical Engineering, TOBB University of Economics and Technology, Ankara, 06560, Turkey
[b] Department of Automotive Engineering, Gazi University, Ankara, 06590, Turkey
[c] College of Engineering and Technology, American University of the Middle East, Eqaila, 15453, Kuwait

ABSTRACT

In this paper, we evaluate various multi-cell design concepts to optimize the crash performances of thin-walled aluminum tubes. The crash performances of the tubes are evaluated by means of two metrics: the crush force efficiency (CFE) and the specific energy absorption (SEA). The CFE and SEA of the tubes are predicted through the use of the finite element analysis software LS-DYNA. Experiments are also conducted to validate the finite element models. Thirty different multi-cell design concepts are evaluated in terms of CFE and SEA, and the best design concept is selected for further evaluation. Next, we perform surrogate-based optimization of the selected design concept, upon which we find that optimum design for maximum CFE which utilizes smaller wall thickness values (except the wall thickness of the inner tube) and larger tube diameters than those of the corresponding ones for the optimum design for maximum SEA. Additionally, the optimized designs exhibit remarkable CFE and SEA performances.

1. Introduction

In the context of automobile design, the energy absorbing elements located behind the vehicle bumper are mainly responsible for the safety of both passengers and critical vehicle components. In case of a frontal collision, these elements deform plastically and transform the crash energy into strain energy through structural deformation. Although many different types of energy absorbers exist, thin-walled tubes are the most commonly used energy absorbing elements as they offer the benefits of low weight, low cost, and ease of production.

The crashworthiness design of thin-walled tubes has been extensively explored via analytical, numerical, and experimental techniques. Alexander [4]'s pioneering study proposed a closed-form formula to predict the mean crushing force. Furthermore, Wierzbicki and Abramowicz [33] introduced the folding of thin-walled tubes as a mechanism for energy absorption, and a super folding element model was developed to evaluate the crash performance of the tubes under quasi-static and dynamic loading conditions [1,2,26]. Sun et al. [29] compared multi-cell empty and foam-filled tubes and determined that the latter afforded better performance in terms of energy absorbing ability. In their comparison of single-cell and 3 × 3 multi-cell square tubes, Zhang et al. [40] found that the multi-cell tube affords 50% more specific energy absorption capacity relative to the single-cell tube. Qiu

et al. [24] performed crashworthiness investigations of multi-cell hexagonal tubes under multiple loading cases and found that multi-cell tubes are more effective than single-cell tubes.

Certain other studies have shown that multi-cell cross sections can improve the crash performance of thin-walled crush tubes [7,9,19,25,32,42–45]. Here, we note that these multi-cell designs are based on simple cell configurations.

Meanwhile, multi-cell tubes with complicated cross-sections have also been investigated. Chen et al. [10] proposed a novel octagonal multi-cell tube with functionally graded thickness to maximize the specific energy absorption and minimize the initial peak force. Xiang and Du [36] considered the microstructure of beetle forewings to design a bio-inspired honeycomb structure and demonstrated the superior energy absorption capacity of this structure relative to conventional multi-cell designs. Pirmohammad and Marzdashti [22] performed optimization of multi-cell tubes with a straight outer tube and tapered inner tube to maximize the specific energy absorption and minimize the initial peak force. Yang et al. [38] proposed the use of multi-cell tubular structures with pre-folded origami patterns to increase the energy absorption capacity.

Zhang and Zhang [39] conducted experiments and numerical simulations on multi-cell tubes with different cross-sections. They found that S4 and S5 multi-cell tubes are considerably more efficient in terms

of specific energy absorption than single-cell tubes; on average, the S4 and S5 multi-cell tubes improve the specific energy absorption by 120% and 220%, respectively, relative to single-cell tubes. Chen et al. [11] reported that a new type of five-cell tube exhibited excellent crashworthiness performance over other tube cross-sections. They further reported that C5C tubes afford a specific energy absorption capacity that is 11.6% greater than that of the C5S tube. Zhang et al. [41] proposed novel bionic multi-cell tubes with quadrilateral, hexagonal, and octagonal profiles. Their numerical analysis revealed that the O-BMCT-6 tube exhibited better crashworthiness performance than other tubes. Xiang et al. Xiang et al. [37] investigated the energy absorption performance of novel multi-cell, polygonal, and honeycomb tubes, and they found that the energy absorption capacity of multi-cell tubes depends on the number of cells. Luo and Fan [18] performed an experimental study on the crushing behavior of rectangular multi-cell tubes and their crashworthiness performance. They found that rectangular multi-cell tubes afford a greater mean crushing force than regular tubes. Pirmohammad and Marzdashti [21] studied the crashworthiness performance of multi-cell thin-walled structures under quasi-static axial and oblique impact loads. Subsequently, they compared different multi-cell structures with triangular, square, hexagonal, and circular cross-sections, and they found that the best crashworthiness performance was afforded by the multi-cell member with the inner tube and scale number of 0.5. Nia and Parsapour [20] presented comparative studies on the crashworthiness performance of simple and multi-cell tubes made of triangular, square, hexagonal, and octagonal sections. Subsequently, they compared their experimental results with their analysis results and found that the hexagonal tubes absorb more energy than the other tubes.

Recent studies have successfully employed different optimization methods to reduce the computational cost of crashworthiness optimization of multi-cell tubes [11,12,23,24,27,28,31]. Hou et al. [15] optimized multi-cell cross-sectional thin-walled tubes with equal sized cells and they found that increasing the number of cells increased the specific energy absorption. Kim [17] investigated a new multi-cell aluminum profile that afforded increased energy absorption 190% over conventional single profiles when considering the parameters of energy absorption and weight efficiency. Wu et al. [35] investigated the influence of the number of cells and topological configurations on the energy absorption of various multi-cell configurations. They found that the five-cell multi-cell tube configuration offers the best crashworthiness characteristics.

Against this backdrop, here, we evaluate 30 different novel geometrically complicated multi-cell design concepts to optimize the crash performances of thin-walled aluminum tubes. This paper is organized as follows: Section 2 provides the geometrical details of the novel multi-cell design concepts investigated in this study. Section 3 presents the details of the finite element modeling of the tubes, followed by the experimental validation of the finite element models in Section 4. The multi-cell design concepts are evaluated in terms of crush force efficiency and specific energy absorption, and Section 5 presents the performance evaluation of these design concepts. Based on the results presented in Section 5, the two best design concepts are selected for further evaluation. Next, mesh verification is demonstrated in Section 6. Surrogate based optimization of the selected design concepts is reported in Section 7, and the optimization results are presented in Section 8. Section 9 concludes the paper.

2. Multi-cell design concepts

In this study, we evaluated 10 different cellular inner patterns (denoted C1 to C10) with 3 different outer cross-sections, namely circular (CIR), double-truncated ellipse (DTE), and square (SQU). Overall, 30 different novel multi-cell design concepts were considered, as listed in Tables 1 and 2. All of these designs are made of 6063-T5 aluminum material, which is suitable of extrusion process provided that the proper

Table 1
First fifteen different novel multi-cell design concepts evaluated.

Table 2
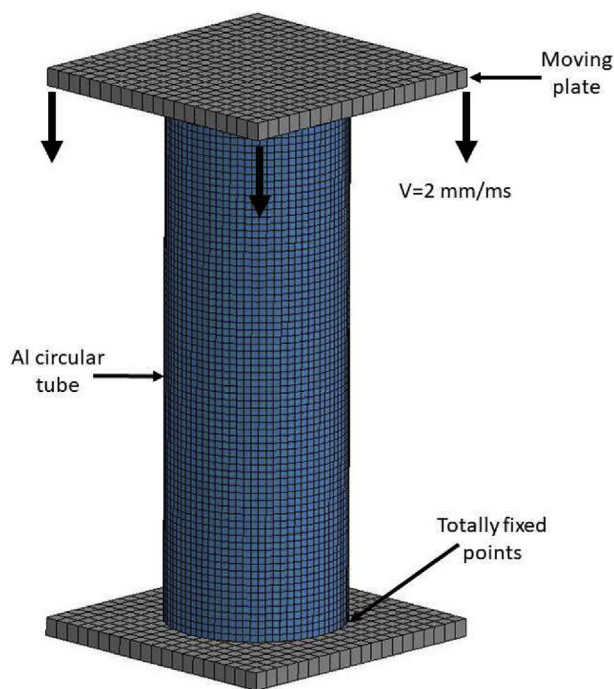Second fifteen different novel multi-cell design concepts evaluated.

Fig. 1. The boundary and impact conditions.

molds are designed and produced.

3. Finite element modeling

The crash responses of the thin-walled tubes under axial loading were analyzed by means of the nonlinear explicit finite element analysis (FEA) software LS-DYNA [14]. The finite element (FE) model, the relevant boundary and impact conditions are shown in Fig. 1. The FE model is composed of three parts: the moving plate, aluminum circular tube, and fixed plate. In the FE simulations, both the moving plate and the fixed plate are modeled as rigid walls (via application of MAT-RIGID in LS-DYNA). The moving plate is assigned a downward velocity of 2 mm/ms to crush the tubes over the fixed plate. Generally, the finite element analysis gives acceptable results when the velocity is ramped to the final value within a certain amount of time. Based on the study conducted by Ahmad and Thambiratnam [3]; this ramping time is selected to be 50 ms, which is the half of the total termination time. Therefore, in our FE analysis, the velocity of the moving plate is ramped up from 0 to 2 mm/ms during the first 50 ms.

The tubes are made of aluminum 6063-T5 with an initial yield stress of $\sigma_Y = 180$ MPa, Youngs modulus of E = 68.9 GPa, Poisson's ratio of $\nu = 0.3$, and density of $\rho = 2700$ kg/m^3 [35]. The true stress-true effective plastic strain data values for aluminum 6063-T5 are listed in Table 3. The material model used is "MAT 24 PIECEWISE LINEAR PLASTICITY" and the tubes are modeled with four-noded shell elements based on Belytschko-Tsay element formulation with five integration points through the thickness. MAT 24 PIECEWISE LINEAR PLASTICITY material model is a widely used model in automotive industry, particularly in crash simulations [8,12,16,30].

For the contact definitions, the automatic single surface contact algorithm is used to define the self-contact of the tubes, and the contact between the tube and the rigid wall; the static and dynamic friction
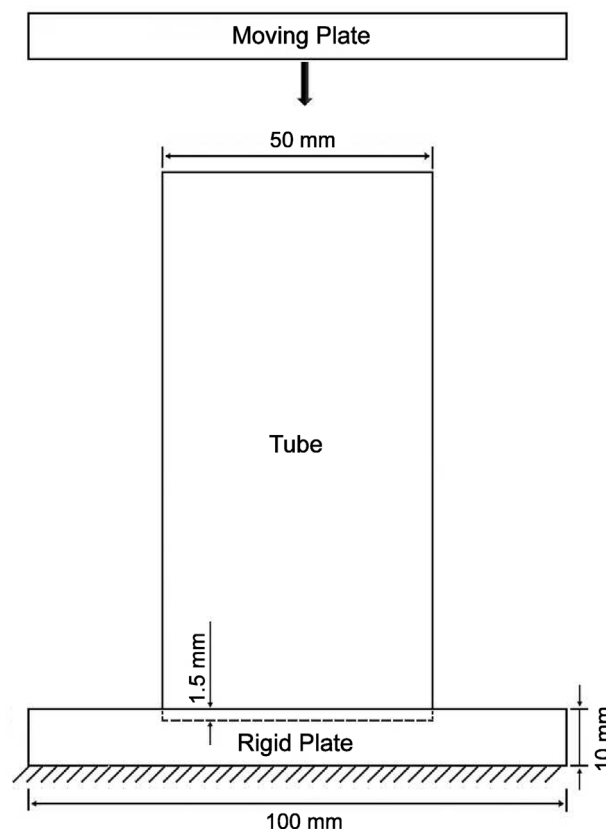

Fig. 2. Base plate used in the test setup.

coefficients for the tubes are assumed to be 0.3 and 0.2 respectively [5,6]. The friction coefficient between the circular tube and the moving rigid plate is taken to be 0.3 [5,6].

4. Experimental validation

In order to validate the finite element model, we conducted three experiments. A single–cell specimen with a circular cross-section and diameter of 50 mm, thickness of 2 mm, and length of 150 mm was prepared. The tests were conducted at the Technology Center of the TOBB University of Economics and Technology, using the INSTRON tensile testing machine with a 60 ton-capacity; this machine was operated at the rate of 2 mm/min. It should be noted that the simulations were performed at higher speeds (2 mm/ms) than the experiments. However, the speed in the simulations was selected such that inertial effects did not contribute to the overall results. The specimens were positioned within the machine such that a 1.5 mm deep groove was formed with a CNC machine on a circular steel plate. In the experiments, one side of the circular tube used was fixed to the ground using by means of a rigid plate, as shown in Fig. 2. The experiments were considered as complete when the rigid plate deformed the specimens by 100 mm.

Fig. 3 shows the deformation process at the beginning of the experiment, when the specimen exhibits the first knuckle, and at the end of the experiment when the specimen is compressed by 100 mm.

Fig. 4 compares the force–displacement results obtained from the experiment (blue line) and the FEA (orange line). The peak crush force

Table 3
True effective stress-true effective plastic strain values for aluminum 6063-T5 (Wu et al., 2016).

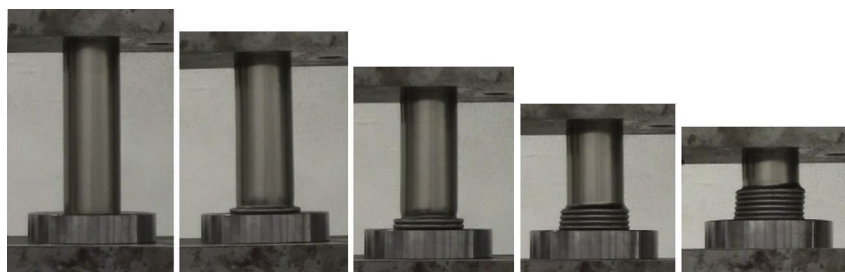| σ_t [MPa]	180	183	189	196	204	212	218	222	231	239	245
ε_p	0.0	0.006	0.011	0.016	0.023	0.031	0.038	0.044	0.057	0.071	0.084

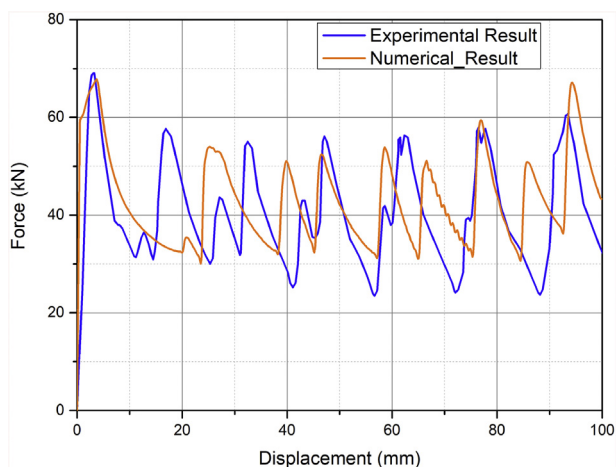**Fig. 3.** The deformation process of the cylindrical tube.

Fig. 4. Force-displacement curves for circular tube.

for the experimental and FEA results are nearly identical (around 70 kN). We also note that the lobe formation observed in the experiments and the FE analysis are similar (Fig. 5). Thus, we conclude that the FEA results are adequately consistent with the experimental results. For single-cell circular tubes, the energy absorption capacity obtained

from the experiments and FE simulations are 4.036 kJ and 4.106 kJ, respectively.

5. Performance evaluation of multi-cell design concepts

The crush performances of the thin-walled tubes are typically assessed using the following energy-based metrics: crush force efficiency, effective crush distance, load uniformity, specific energy absorption, and usage ratio Fang et al. [13]. In this study, we considered crush force efficiency (CFE), and specific energy absorption (SEA).

The energy absorption (EA) of a thin-walled tube can be determined by integrating the crushing force with respect to the displacement as follows:

$$EA = \int_0^d F(x)dx \tag{1}$$

where d denotes the deformation distance and F the crushing force. The parameter SEA is defined as the absorbed energy per unit mass. That is, SEA can be computed as:

$$SEA = \frac{EA}{m} \tag{2}$$

where m denotes the mass of the tube.

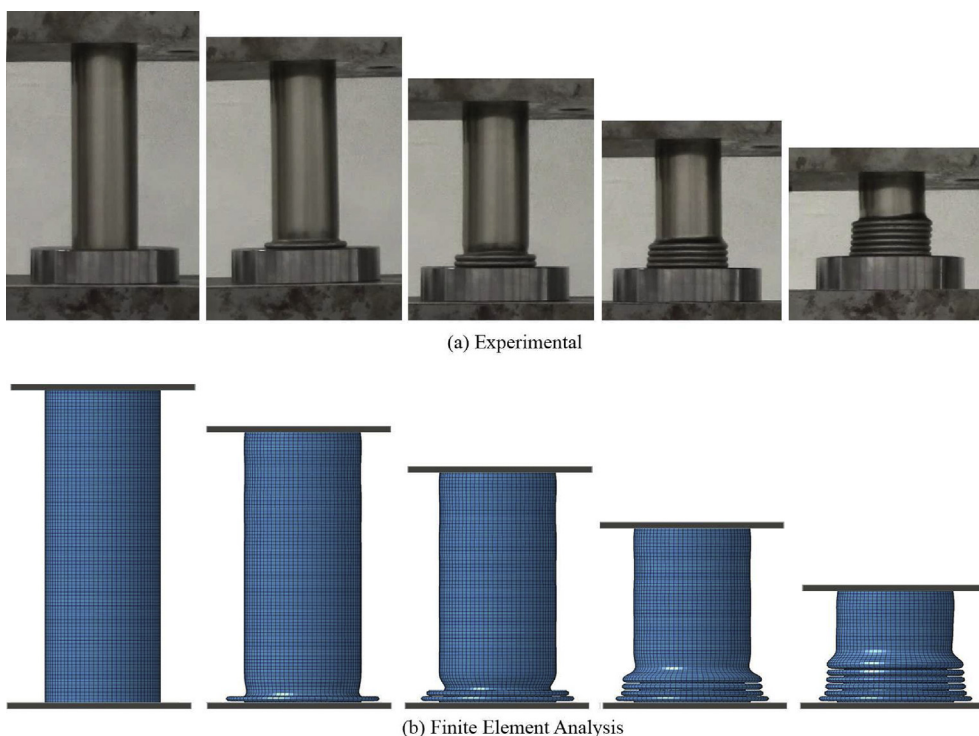Parameter CFE is defined as the ratio of the mean crush force (MCF)

(a) Experimental

(b) Finite Element Analysis

Fig. 5. The lobe formation comparison of experiments and FE analysis.

Table 4
Crash performance evaluation of the multi-cell design concepts.

Concept	EA (kJ)	PCF (kN)	MCF (kN)	CFE	SEA (kj/kg)	F
C1-CIR	8.777	99.02	87.77	0.886	37.67	1.556
C1-DTE	8.210	100.37	82.10	0.818	26.22	1.309
C1-SQU	8.159	104.54	81.59	0.780	28.07	1.294
C2-CIR	11.494	136.75	114.94	0.841	35.44	1.471
C2-DTE	12.694	146.95	126.94	0.864	31.29	1.436
C2-SQU	11.394	135.81	113.94	0.839	28.69	1.369
C3-CIR	9.541	120.58	95.41	0.791	38.36	1.460
C3-DTE	10.947	122.45	109.47	**0.894**	34.09	1.512
C3-SQU	10.933	131.31	109.33	0.833	36.94	1.485
C4-CIR	24.355	309.24	243.55	0.788	**67.24**	**1.885**
C4-DTE	21.000	268.25	210.00	0.783	47.05	1.579
C4-SQU	20.216	233.54	202.16	0.866	49.28	1.706
C5-CIR	20.975	243.34	209.75	0.862	41.87	1.591
C5-DTE	20.364	257.40	203.64	0.573	45.67	1.323
C5-SQU	21.477	248.85	214.77	0.863	40.76	1.576
C6-CIR	26.982	409.92	269.82	0.658	40.84	1.347
C6-DTE	24.471	355.16	244.71	0.689	35.82	1.307
C6-SQU	24.771	364.10	247.71	0.680	36.75	1.311
C7-CIR	20.260	234.26	202.60	0.865	52.16	1.748
C7-DTE	25.197	290.49	251.97	0.867	50.27	1.722
C7-SQU	22.130	264.22	221.30	0.838	47.91	1.654
C8-CIR	7.284	88.30	72.84	0.825	31.60	1.397
C8-DTE	8.519	103.04	85.19	0.827	28.97	1.360
C8-SQU	8.544	101.95	85.44	0.838	31.64	1.412
C9-CIR	13.984	197.10	139.84	0.709	40.72	1.403
C9-DTE	12.523	154.59	125.23	0.810	28.45	1.333
C9-SQU	13.278	166.76	132.78	0.796	30.79	1.352
C10-CIR	13.553	165.17	135.53	0.821	37.88	1.485
C10-DTE	18.291	218.83	182.91	0.836	36.48	1.482
C10-SQU	15.550	180.57	155.50	0.861	34.69	1.484

to the peak crush force (PCF). That is, CFE can be computed as:

$$CFE = \frac{MCF}{PCF} \tag{3}$$

$$MCF = \frac{1}{d} \int_0^d F(x)dx = \frac{EA}{d} \tag{4}$$

$$PCF = \max_{0 \leq x \leq d} F(x) \tag{5}$$

Table 4 lists the crash performances of the tubes in terms of CFE and SEA. The best CFE performance is achieved by the C3-DTE design, whereas the best SEA performance is achieved by the C4-CIR design. To balance the CFE and SEA performances, we define a composite objective function F as follows:

$$F = \omega_1 \frac{CFE}{CFE_{max}} + \omega_2 \frac{SEA}{SEA_{max}} \tag{6}$$

where ω_1 and ω_2 are the weighting factors related to CFE and SEA optimization. Moreover, CFE_{max} and SEA_{max} represent the maximum CFE and SEA values, respectively, observed amongst the 30 novel designs investigated in this study. Since we give equal importance to CFE maximization and SEA maximization, the weighting factors ω_1 and ω_2 are taken equal to one. From Table 4, we find that the C4-CIR design affords the best composite objective function value. In order to provide a general idea for the deformation mechanism of different multi-cell design concepts, we provided the deformation plots in the revised manuscript (see Fig. 6). When the impact loads are compared, we see that C6-CIR design has 409.9 kN impact load at 100 mm deformation. If such a high impact load is transferred to the passenger, it introduces high risk of head or neck injury to the passenger. When the deformation mechanisms are explored, we see that C6-SQU design has the best lobe formation characteristic. If a crashbox has a good lobe formation characteristic, then the force transferred from the crashbox to the neighboring parts would be evenly distributed. However, this does not guarantee the largest specific energy absorption performance. When the
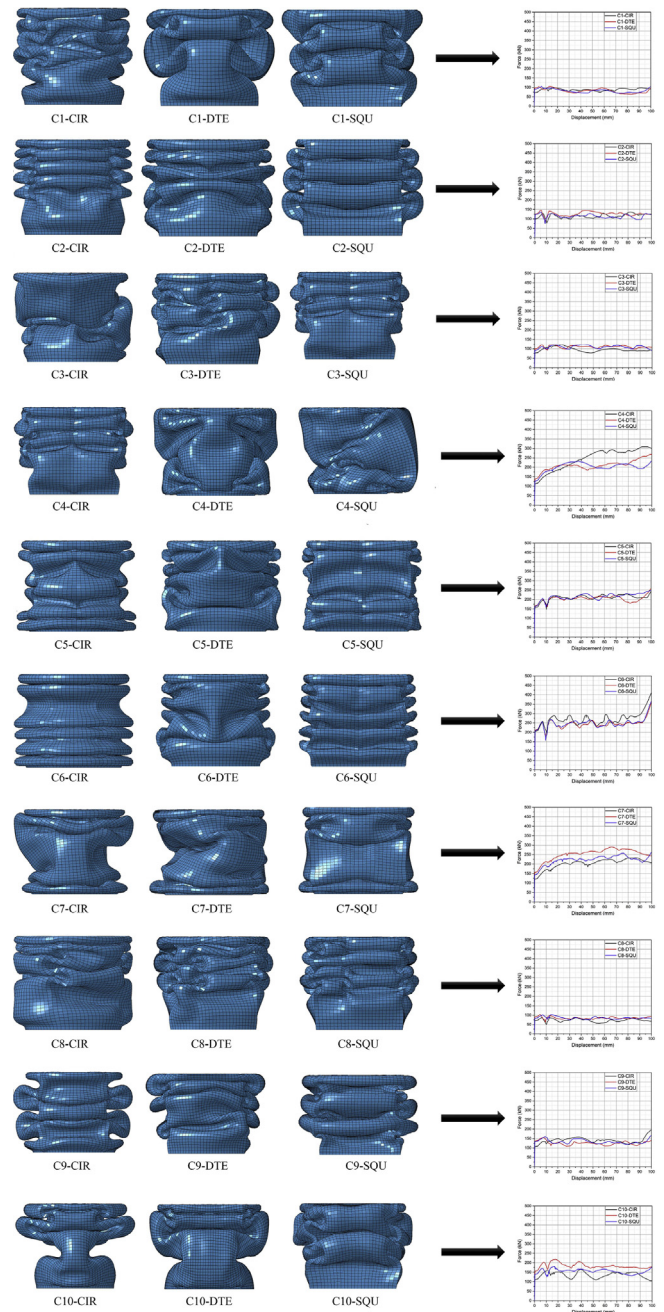

Fig. 6. Collapse behavior observed during the deformation of the tubes.

specific energy absorption values are compared, we observe that C4-CIR design has 67.24 kJ/kg of SEA value, which is 29% larger than that of the C7-CIR design that has the second best SEA value. Therefore, the C4-CIR design concept is selected for further evaluation.

6. Mesh verification for C4-CIR design

After the selection of C4-CIR design as the baseline model, we next determined the appropriate mesh size for this design concept before the optimization process. The appropriate mesh size was determined based on the variation of the mean crush force with respect to the mesh size. The C4-CIR design was meshed with different mesh sizes (4.0, 3.5, 3.0, 2.5 and 2.0 mm) and we attempted to find the mesh size that afforded convergence of the mean crash force. From Table 5 and Fig. 7 observe that mesh convergence is obtained for a mesh size of 2.5 mm. Therefore, this mesh size was used in subsequent simulations conducted for

Table 5
Verification of the mesh size for C4-CIR.

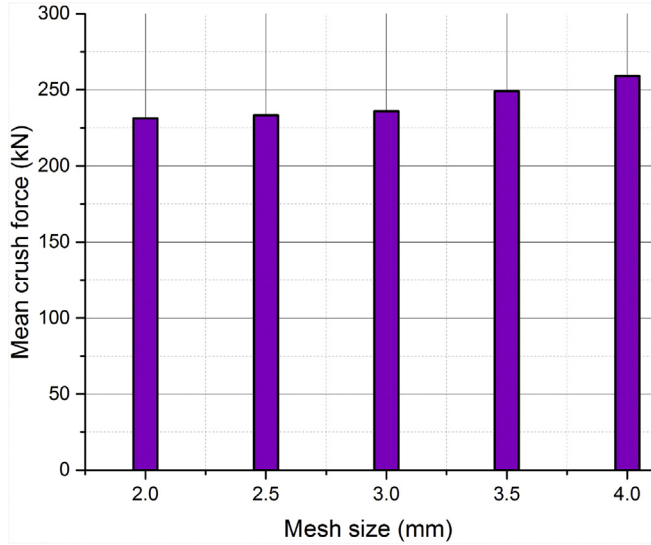| Mesh Size (mm)	Displacement (mm)	EA (kJ)	PCF (kN)	MCF (kN)	CFE	SEA (kJ/kg)
2.0	100.00	23.12	242.7	231.2	0.951	48.17
2.5	100.00	23.32	271.6	233.2	0.860	49.62
3.0	100.00	23.59	295.6	235.9	0.801	49.15
3.5	100.00	24.91	305.2	249.1	0.823	51.90
4.0	100.00	25.90	361.9	259.0	0.721	53.96

Fig. 7. Mean crush force versus mesh size for C4-CIR design.

optimization.

7. Surrogate based optimization

7.1. Description of model geometry

The details of the model geometry for the C4-CIR design are shown in Fig. 8. This design has a tri-tubular geometry. All the tubes have the same length of $L = 150$ mm. The diameter of the outer tube D_o, diameter of the middle tube D_m, and diameter of the inner tube D_i as well as the wall thicknesseses t_1 through t_5 were selected as design variables for the optimization process.

7.2. Formulation of optimization problem

The optimization problem for the C4-CIR tubes can be stated as

$$
\begin{aligned}
&\text{Find} && D_0, D_m, D_i, t_1, t_2, t_3, t_4, t_5 \\
&\text{Min} && f \\
&\text{Such that} && 30 \text{ mm} \leq D_0 \leq 70 \text{ mm} \\
& && 0.3D_0 \leq D_m \leq 0.7D_0 \\
& && 0.3D_m \leq D_i \leq 0.7D_m \\
& && 1 \text{ mm} \leq t_1, t_2, t_3, t_4, t_5 \leq 3 \text{ mm}
\end{aligned}
\tag{7}
$$

where the objective function f is set as $f = -CFE$ to design the tubes for maximum CFE, and $f = -SEA$ to design the tubes for maximum SEA.

The optimization problem stated above can be solved by means of the surrogate-based approach. Gaussian process (GP) models are normally constructed to relate the crashworthiness responses to the design variables. In this study, we used the Gaussian process code from Williams and Rasmussen Williams and Rasmussen [34]. The constructed GP models were integrated into MATLAB's "fmincon" built-in function that uses sequential quadratic programming. To ensure global
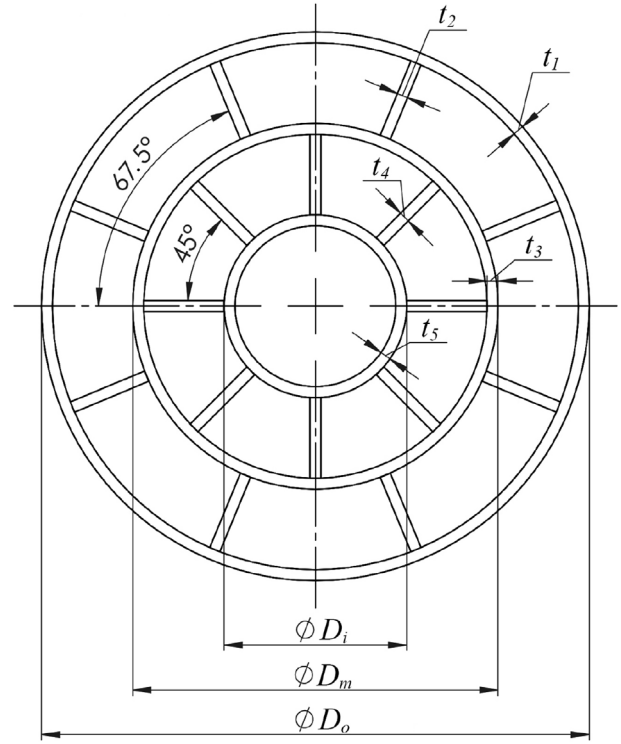

Fig. 8. The geometric details of the circular tube.

convergence, the optimization runs used 100 different starting points.

7.3. GP models

The GP assumes that the output variables $f_N = \{f_n(x_n^1, x_n^2, \cdots, x_n^L)\}_{n=1}^N$ are related to each other via a Gaussian joint probability distribution

$$
P(f_N | C_N, X_N) = \frac{1}{\sqrt{(2\pi)^N |C_N|}} \exp\left[-\frac{1}{2}(f_N - \mu)^T C_N^{-1}(f_N - \mu) \right]
\tag{8}
$$

where $X_N = \{x_n\}_{n=1}^N$ are N pairs of L-dimensional input variables $x_n = (x_n^1, x_n^2, \cdots, x_n^L)$, C_N is the covariance matrix with elements of $C_{ij} = C(x_i, x_j)$, and μ is the mean output vector. The GP estimates the output at a prediction point $\mathbf{x}_p = (\mathbf{x}_p^1, \mathbf{x}_p^2, \cdots, \mathbf{x}_p^L)$ as

$$
\hat{f}(\mathbf{x}_p) = k^T C_N^{-1} f_N
\tag{9}
$$

where $k = [C(x_1, x_p), \cdots, C(x_N, x_p)]$. One of the advantages of the GP is that the standard deviation at the prediction point is readily available without a requirement of any extra simulations. This standard deviation can be utilized as an error measure and can be calculated as

$$
\sigma_{\hat{f}(\mathbf{x}_p)} = \kappa - k^T C_N^{-1} k
\tag{10}
$$

where $\kappa = C(x_p, x_p)$.

We notice from Eq. (9) that the GP prediction depends on the covariance matrix C_N. The elements of this matrix are calculated either from Eq. (11) or Eq. (12) depending on the use of the GP model. The covariance function given in Eq. (11) defines the interpolation mode of the GP model that passes through all the training data points exactly. On the other hand, the covariance function given in Eq. (12) defines the regression mode of the model, which allows us to build smoother surfaces for problems with noisy data. Once the noise of the output values is filtered out, the prediction model becomes less complex and but it may not pass through all the training points. However, it provides a better prediction at the non-training points [34].

$$C_{ij} = \theta_1 \exp\left[-\frac{1}{2}\sum_{l=1}^{L}\frac{(x_i^{(l)} - x_j^{(l)})^2}{\eta_l^2}\right] + \theta_2 \tag{11}$$

$$C_{ij} = \theta_1 \exp\left[-\frac{1}{2}\sum_{l=1}^{L}\frac{(x_i^{(l)} - x_j^{(l)})^2}{\eta_l^2}\right] + \theta_2 + \delta_{ij}\theta_3 \tag{12}$$

Here θ_1, θ_2, θ_3, and η $(l = 1,2,\cdots,L)$ are called "hyperparameters". Further δ_{ij} is the Kronecker delta and θ_3 is an independent noise parameter. The hyperparameters are selected so as to maximize the logarithmic likelihood that the model prediction matches the training response data. The logarithmic likelihood function L can be expressed as:

$$L = -\frac{1}{2}\log|C_N| - \frac{1}{2}f_N^T C_N^{-1} f_N - \frac{N}{2}\log 2\pi + \ln P(\theta) \tag{13}$$

where $P(\theta)$ represents the prior distribution of the hyperparameters. In most of the applications, there is no prior knowledge of the values of the hyperparameters, so the prior distribution is uniform. Consequently, the last term of Eq. (13), $\ln P(\theta)$, becomes a constant and can be considered as zero for the purpose of optimization, as we did in this work.

The covariance function given in by Eq. (11) defines the interpolation mode of the GP metamodel, that passes through all the training data points exactly. On the other hand, the covariance function given in Eq. (12) defines the regression mode of the model, which allows us to build smoother surfaces for problems with noisy data. Once the noise of the output values is filtered out, the prediction model becomes less complex, and but it may not pass through all the training points. However, it provides a better prediction at the non-training points [34].

7.4. Construction of GP models

The GP models were used to predict responses of interest through regression of the response data obtained at some training points, as described in the previous sub-section. The training points were selected by use of a design of experiments (DOE) technique. In this study, the Latin hypercube sampling DOE type was used to generate 200 training points within the bounds of the input design variables. Next, the responses were computed at the training points to generate a set of response values. Finally, the training points and the corresponding set of response values were used to fit a GP model that can be used to estimate the value of response at any arbitrary point in the input design space.

7.5. Accuracy of GP models

The accuracies of the constructed GP models are evaluated through two error metrics: (i) the leave-one-out generalized root mean square cross validation error, GMSE, evaluated at the training points, and (ii) the root mean square error, RMSE, evaluated at the test points.

The GMSE computed at the training points is calculated as follows. If there are N training points, GP models are constructed N times, each time leaving out one of the training points. Next, the difference between the exact value of the response y_k at the omitted training point x_k and the predicted value of the response using the GP model $\hat{y}_k^{(-k)}$ is calculated. Finally, the GMSE is calculated as

$$GMSE = \sqrt{\frac{1}{N}\sum_{k=1}^{N}(y_k - \hat{y}_k^{(-k)})^2} \tag{14}$$

The GMSE can be normalized with the mean value of the response to yield

$$GMSE_{nor} = \frac{GMSE}{\frac{1}{N}\sum_{k=1}^{N}y_k} \tag{15}$$

The RMSE computed at the test points is calculated as follows. Fifty test points are generated through random sampling and the responses at these test points are evaluated. Subsequently, the RMSE is calculated as

Table 6
Normalized GMSE errors of the GP models constructed for CFE and SEA.

	GMSE$_{nor}$	RMSE$_{nor}$
CFE	8.5	7.8
SEA	16.7	12.2

$$GMSE = \sqrt{\frac{1}{N_t}\sum_{k=1}^{N_t}\left[(\hat{y}_{pred})_k - (y_{test})_k\right]^2} \tag{16}$$

where N_t represents the number of test points, $(\hat{y}_{pred})_k$ the GP prediction of the response at the k'th test point, and $(y_{test})_k$ the actual value of the response at the k'th test point.

The RMSE can also be normalized with the mean value of the response to yield

$$RMSE_{nor} = \frac{RMSE}{\frac{1}{N}\sum_{k=1}^{N}y_k} \tag{17}$$

The normalized GMSE and RMSE values of the GP models constructed for CFE and SEA response predictions are listed in Table 6. We note that the GP models constructed for CFE predictions are more accurate than the ones constructed for SEA predictions. It can also be observed that the GMSE values are larger than RMSE values as expected. The error values listed in Table 6 are acceptable for response prediction of a highly nonlinear phenomenon such as a crash.

8. Optimization results

Table 7 lists the optimum values of the design variables, CFE value of the optimum design predicted by the GP model, CFE value of the optimum design computed through FEA, and percent error in the CFE prediction for the optimum design for maximum CFE. Similarly, Table 8 lists the optimum values of the design variables, SEA value of the optimum design predicted by the GP model, SEA value of the optimum design computed through FEA, and percent error in SEA prediction for the optimum design for maximum SEA.

It can be observed that the error in the GP prediction of the CFE of the optimum design for maximum CFE is 7.4%, and the error in the GP prediction of the SEA of the optimum design for maximum SEA is − 4.4%.

Upon comparing the optimization results presented in Tables 7 and 8, we observe that smaller wall thickness values (except the wall thickness of the inner tube) and larger tube diameters are used in the optimum design for maximum CFE than the corresponding ones in the optimum design for maximum SEA. Fig. 9 shows the comparison of the folding patterns between the baseline and the best design models.

Finally, Table 9 shows the optimum values of the design variables, the GP model predictions of CFE, SEA and F, the FEA results of CFE, SEA and F, and the percent error in CFE, SEA and F prediction for the optimum design for maximum composite objective function F. It is seen that the error in CFE prediction is 5.5%, the error in SEA prediction is 1.9%, and the error in F prediction is 3.1%. Recall that the F value of the C4-CIR design before optimization was 1.885 (see Table 4), and it is increased to 2.116 through optimization (12% improvement).

9. Conclusions

In our study, we evaluated various multi-cell design concepts to optimize the crash performances of thin-walled aluminum tubes. The crash performances of the tubes were evaluated by means of two metrics: CFE, and SEA. The CFE and SEA values of the tubes were predicted by using the FEA software LS-DYNA. Experiments were also conducted to validate the finite element models. Thirty different multi-cell design concepts were evaluated in terms of CFE and SEA and the best design concept was subsequently selected for further evaluation.
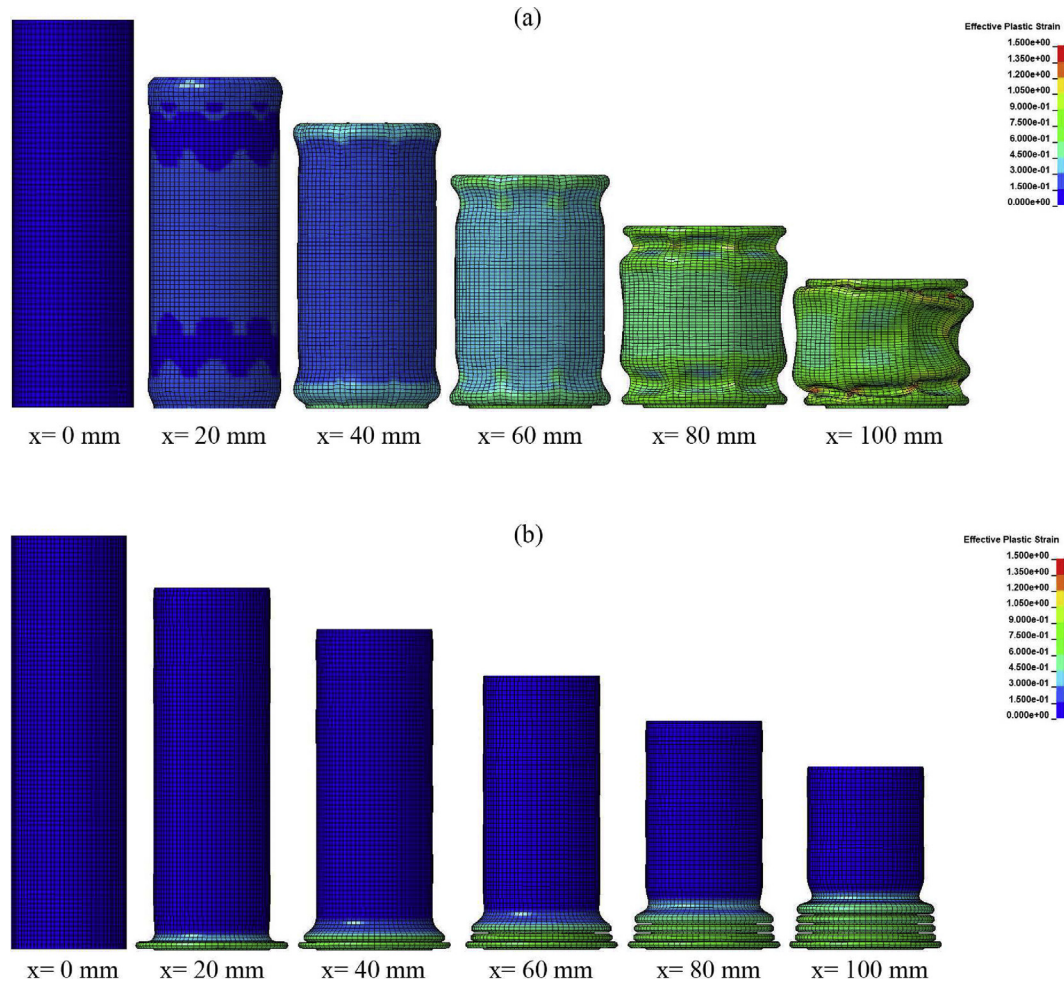
Table 7
Optimization results for maximum CFE.

t_1 [mm]	t_2 [mm]	t_3 [mm]	t_4 [mm]	t_5 [mm]	D_o [mm]	D_m [mm]	D_i [mm]	CFE (pred.)	CFE (FEA)	% error
1.000	2.579	1.609	1.000	1.235	63.96	19.19	10.22	0.874	**0.814**	7.4

Table 8
Optimization results for maximum SEA.

t_1 [mm]	t_2 [mm]	t_3 [mm]	t_4 [mm]	t_5 [mm]	D_o [mm]	D_m [mm]	D_i [mm]	SEA[a] (pred.)	SEA[a] (FEA)	% error
2.664	3.000	3.000	2.607	1.101	46.48	15.07	6.55	104.39	**109.23**	−4.4

[a] SEA is in kJ/kg.

Fig. 9. Folding patterns of tubes a) best design b) baseline (x is the deformation distance).

Table 9
Optimization results for the composite function F.

Optimum values of the design variables							
t_1 [mm]	t_2 [mm]	t_3 [mm]	t_4 [mm]	t_5 [mm]	D_o [mm]	D_m [mm]	D_i [mm]
2.872	3.000	1.000	1.000	3.000	45.41	14.10	9.87
Corresponding response predictions							
CFE (pred.)	CFE (FEA)	% error	SEA (pred.)	SEA(FEA)	% error	F (pred.)	F (FEA)	% error
0.6922	0.6563	5.5	94.44	92.71	1.9	2.179	2.113	3.1

Surrogate based optimization of the selected design concept was performed. From our results obtained in this study, the following conclusions were drawn.

- The accuracies of the constructed GP models were evaluated by using the leave-one-out generalized root mean square cross validation error, GMSE, evaluated at the training points, and the root mean square error, RMSE, evaluated at the test points. It was observed that the GMSE values were larger than RMSE values, as expected.
- The GP models constructed for CFE predictions were more accurate than the ones constructed for SEA predictions.
- The normalized RMSE values of the GP models constructed for CFE and SEA predictions were 7.8% and 12.2%, respectively, and these errors were found to be acceptable for response prediction of a highly nonlinear phenomenon such as a crash.
- The errors of the GP models evaluated for the optimum designs were smaller compared with the global accuracies of the GP models. The error in GP prediction of the CFE of the optimum design for maximum CFE was 7.4%, and the error in GP prediction of the SEA of the optimum design for maximum SEA was −4.4%.
- Optimization results showed that smaller wall thickness values (execpt the wall thickness of the inner tube) and larger tube diameters were utilized in the optimum design for maximum CFE when compared with the corresponding ones in the optimum design for maximum SEA.

Acknowledgements

Appendix A. Supplementary data

Supplementary data to this article can be found online at https://doi.org/10.1016/j.tws.2019.05.012.

References

[1] W. Abramowicz, N. Jones, Dynamic progressive buckling of circular and square tubes, Int. J. Impact Eng. 4 (4) (1986) 243–270.
[2] W. Abramowicz, Thin-walled structures as impact energy absorbers, Thin-Walled Struct. 41 (2–3) (2003) 91–107.
[3] Z. Ahmad, D. Thambiratnam, Crushing response of foam-filled conical tubes under quasi-static axial loading, Mater. Des. 30 (7) (2009) 2393–2403.
[4] J.M. Alexander, An approximate analysis of the collapse of thin cylindrical shells under axial loading, Q. J. Mech. Appl. Math. 13 (1) (1960) 10–15.
[5] M. Altin, M.A. Güler, S.K. Mert, The effect of percent foam fill ratio on the energy absorption capacity of axially compressed thin-walled multi-cell square and circular tubes, Int. J. Mech. Sci. 131 (2017) 368–379.
[6] M. Altin, E. Acar, M. Güler, Foam filling options for crashworthiness optimization of thin-walled multi-tubular circular columns, Thin-Walled Struct. 131 (2018) 309–323.
[7] M. Altin, Ü. Kılınçkaya, E. Acar, M.A. Güler, Investigation of combined effects of cross section, taper angle and cell structure on crashworthiness of multi-cell thin-walled tubes, Int. J. Crashworthiness 24 (2) (2019) 121–136.
[8] X. An, Y. Gao, J. Fang, G. Sun, Q. Li, Crashworthiness design for foam-filled thin-walled structures with functionally lateral graded thickness sheets, Thin-Walled Struct. 91 (2015) 63–71.
[9] W. Chen, T. Wierzbicki, Relative merits of single-cell, multi-cell and foam-filled thin-walled structures in energy absorption, Thin-Walled Struct. 39 (4) (2001) 287–306.
[10] Y. Chen, Z. Bai, L. Zhang, Y. Wang, G. Sun, L. Cao, Crashworthiness analysis of octagonal multi-cell tube with functionally graded thickness under multiple loading angles, Thin-Walled Struct. 110 (2017) 133–139.
[11] S. Chen, H. Yu, J. Fang, A novel multi-cell tubal structure with circular corners for crashworthiness, Thin-Walled Struct. 122 (2018) 329–343.
[12] J. Fang, Y. Gao, G. Sun, N. Qiu, Q. Li, On design of multi-cell tubes under axial and oblique impact loads, Thin-Walled Struct. 95 (2015) 115–126.
[13] J. Fang, G. Sun, N. Qiu, N.H. Kim, Q. Li, On design optimization for structural crashworthiness and its state of the art, Struct. Multidiscip. Optim. 55 (3) (2017)
1091–1119.
[14] J.O. Hallquist, LS-DYNA Theory Manual, Livermore Software Technology Corporation, 2016.
[15] S. Hou, Q. Li, S. Long, X. Yang, W. Li, Multiobjective optimization of multi-cell sections for the crashworthiness design, Int. J. Impact Eng. 35 (11) (2008) 1355–1367.
[16] S. Hou, X. Han, G. Sun, S. Long, W. Li, X. Yang, Q. Li, Multiobjective optimization for tapered circular tubes, Thin-Walled Struct. 49 (7) (2011) 855–863.
[17] H.-S. Kim, New extruded multi-cell aluminum profile for maximum crash energy absorption and weight efficiency, Thin-Walled Struct. 40 (4) (2002) 311–327.
[18] Y. Luo, H. Fan, Energy absorbing ability of rectangular self-similar multi-cell sandwich-walled tubular structures, Thin-Walled Struct. 124 (2018) 88–97.
[19] A. Mahmoodi, M. Shojaeefard, H.S. Googarchin, Theoretical development and numerical investigation on energy absorption behavior of tapered multi-cell tubes, Thin-Walled Struct. 102 (2016) 98–110.
[20] A.A. Nia, M. Parsapour, Comparative analysis of energy absorption capacity of simple and multi-cell thin-walled tubes with triangular, square, hexagonal and octagonal sections, Thin-Walled Struct. 74 (2014) 155–165.
[21] S. Pirmohammad, S.E. Marzdashti, Crushing behavior of new designed multi-cell members subjected to axial and oblique quasi-static loads, Thin-Walled Struct. 108 (2016) 291–304.
[22] S. Pirmohammad, S.E. Marzdashti, Crashworthiness optimization of combined straight-tapered tubes using genetic algorithm and neural networks, Thin-Walled Struct. 127 (2018) 318–332.
[23] C. Qi, S. Yang, F. Dong, Crushing analysis and multiobjective crashworthiness optimization of tapered square tubes under oblique impact loading, Thin-Walled Struct. 59 (2012) 103–119.
[24] N. Qiu, Y. Gao, J. Fang, Z. Feng, G. Sun, Q. Li, Crashworthiness analysis and design of multi-cell hexagonal columns under multiple loading cases, Finite Elem. Anal. Des. 104 (2015) 89–101.
[25] N. Qiu, Y. Gao, J. Fang, Z. Feng, G. Sun, Q. Li, Theoretical prediction and optimization of multi-cell hexagonal tubes under axial crashing, Thin-Walled Struct. 102 (2016) 111–121.
[26] S. Santosa, T. Wierzbicki, On the modeling of crush behavior of a closed-cell aluminum foam structure, J. Mech. Phys. Solids 46 (4) (1998) 645–669.
[27] G. Sun, T. Pang, J. Fang, G. Li, Q. Li, Parameterization of criss-cross configurations for multiobjective crashworthiness optimization, Int. J. Mech. Sci. 124 (2017) 145–157.
[28] G. Sun, T. Liu, J. Fang, G.P. Steven, Q. Li, Configurational optimization of multi-cell topologies for multiple oblique loads, Struct. Multidiscip. Optim. 57 (2) (2018) 469–488.
[29] G. Sun, T. Liu, X. Huang, G. Zheng, Q. Li, Topological configuration analysis and design for foam filled multi-cell tubes, Eng. Struct. 155 (2018) 235–250.
[30] G. Sun, M. Deng, G. Zheng, Q. Li, Design for cost performance of crashworthy structures made of high strength steel, Thin-Walled Struct. 138 (2019) 458–472.
[31] T. Tran, S. Hou, X. Han, N. Nguyen, M. Chau, Theoretical prediction and crashworthiness optimization of multi-cell square tubes under oblique impact loading, Int. J. Mech. Sci. 89 (2014) 177–193.
[32] S. Wang, Y. Peng, T. Wang, Q. Che, P. Xu, Collision performance and multi-objective robust optimization of a combined multi-cell thin-walled structure for high speed train, Thin-Walled Struct. 135 (2019) 341–355.
[33] T. Wierzbicki, W. Abramowicz, On the crushing mechanics of thin-walled structures, J. Appl. Mech. 50 (4a) (1983) 727–734.
[34] C.K. Williams, C.E. Rasmussen, Gaussian Processes for Machine Learning vol. 2, MIT Press Cambridge, MA, 2006.
[35] S. Wu, G. Zheng, G. Sun, Q. Liu, G. Li, Q. Li, On design of multi-cell thin-wall structures for crashworthiness, Int. J. Impact Eng. 88 (2016) 102–117.
[36] J. Xiang, J. Du, Energy absorption characteristics of bio-inspired honeycomb structure under axial impact loading, Mater. Sci. Eng.: A 696 (2017) 283–289.
[37] Y. Xiang, T. Yu, L. Yang, Comparative analysis of energy absorption capacity of polygonal tubes, multi-cell tubes and honeycombs by utilizing key performance indicators, Mater. Des. 89 (2016) 689–696.
[38] K. Yang, S. Xu, S. Zhou, Y.M. Xie, Multi-objective optimization of multi-cell tubes with origami patterns for energy absorption, Thin-Walled Struct. 123 (2018) 100–113.
[39] X. Zhang, H. Zhang, Energy absorption of multi-cell stub columns under axial compression, Thin-Walled Struct. 68 (2013) 156–163.
[40] X. Zhang, G. Cheng, H. Zhang, Theoretical prediction and numerical simulation of multi-cell square thin-walled structures, Thin-Walled Struct. 44 (11) (2006) 1185–1191.
[41] L. Zhang, Z. Bai, F. Bai, Crashworthiness design for bio-inspired multi-cell tubes with quadrilateral, hexagonal and octagonal sections, Thin-Walled Struct. 122 (2018) 42–51.
[42] Y. Zhang, X. Xu, G. Sun, X. Lai, Q. Li, Nondeterministic optimization of tapered sandwich column for crashworthiness, Thin-Walled Struct. 122 (2018) 193–207.
[43] Y. Zhang, X. Xu, J. Wang, T. Chen, C.H. Wang, Crushing analysis for novel bio-inspired hierarchical circular structures subjected to axial load, Int. J. Mech. Sci. 140 (2018) 407–431.
[44] G. Zheng, T. Pang, G. Sun, S. Wu, Q. Li, Theoretical, numerical, and experimental study on laterally variable thickness (lvt) multi-cell tubes for crashworthiness, Int. J. Mech. Sci. 118 (2016) 283–297.
[45] G. Zheng, T. Pang, G. Sun, S. Wu, Q. Li, Theoretical, numerical, and experimental study on laterally variable thickness (lvt) multi-cell tubes for crashworthiness, Int. J. Mech. Sci. 118 (2016) 283–297.